HHS Public Access

Author manuscript

Mol Imaging Biol. Author manuscript; available in PMC 2018 April 01.

Published in final edited form as:

Mol Imaging Biol. 2017 April ; 19(2): 194–202. doi:10.1007/s11307-016-0991-4.

Assessment of Molecular Acoustic Angiography for Combined Microvascular and Molecular Imaging in Preclinical Tumor Models

Brooks D. Lindsey[1,*], **Sarah E. Shelton**[1,*], **F. Stuart Foster**[2], and **Paul A. Dayton**[1,3]

[1]Joint Department of Biomedical Engineering, University of North Carolina-Chapel Hill and North Carolina State University, Raleigh, NC, USA

[2]Sunnybrook Health Sciences Centre, Toronto, ON, CA

[3]Biomedical Research Imaging Center, University of North Carolina-Chapel Hill, USA

Abstract

Purpose—To evaluate a new ultrasound molecular imaging approach in its ability to image a preclinical tumor model and to investigate the capacity to visualize and quantify co-registered microvascular and molecular imaging volumes.

Procedures—Molecular imaging using the new technique was compared with a conventional ultrasound molecular imaging technique (multi-pulse imaging) by varying the injected microbubble dose and scanning each animal using both techniques. Each of the 14 animals was randomly assigned one of three doses; bolus dose was varied, and the animals were imaged for three consecutive days so that each animal received every dose.

A microvascular scan was also acquired for each animal by administering an infusion of non-targeted microbubbles. These scans were paired with co-registered molecular images (VEGFR2-targeted microbubbles), the vessels were segmented, and the spatial relationships between vessels and VEGFR2 targeting locations were analyzed. In 5 animals, an additional scan was performed in which the animal received a bolus of microbubbles targeted to E- and P-selectin. Vessel tortuosity as a function of distance from VEGF and selectin targeting was analyzed in these animals.

Results—Although resulting differences in image intensity due to varying microbubble dose were not significant between the two lowest doses, superharmonic imaging had significantly higher contrast-to-tissue ratio (CTR) than multi-pulse imaging (mean across all doses: 13.98 dB for molecular acoustic angiography vs. 0.53 dB for multi-pulse imaging; $p = 4.9 \times 10^{-10}$). Analysis of registered microvascular and molecular imaging volumes indicated that vessel tortuosity decreases with increasing distance from both VEGFR2 and selectin targeting sites.

Conclusions—Molecular acoustic angiography (superharmonic molecular imaging) exhibited a significant increase in CTR at all doses tested due to superior rejection of tissue artifact signals.

Corresponding author: padayton@email.unc.edu, phone: (919) 843-9521, fax: (919) 843-9520.
*Authors contributed equally to this work

Conflict of interest

The authors declare that they have no conflict of interests with any other companies listed in this paper.

Due to the high resolution of acoustic angiography molecular imaging, it is possible to analyze spatial relationships in aligned microvascular and molecular superharmonic imaging volumes. Future studies are required to separate the effects of biomarker expression and blood flow kinetics in comparing local tortuosity differences between different endothelial markers such as VEGFR2, E-selectin and P-selectin.

Keywords

microbubble; superharmonic; microvasculature; angiogenesis; tortuosity; targeted imaging; ultrasound; contrast imaging; VEGFR2; selectin

Introduction

The development of microbubble contrast agents has enabled ultrasound molecular imaging through the use of microbubbles targeted to vascular endothelium [1–5]. Compared to other molecular imaging modalities, ultrasound molecular imaging is lower in cost, provides higher throughput, and does not require the use of ionizing radiation. However, molecular imaging with ultrasound also has relatively low sensitivity to accumulated microbubbles and is subject to false positive artifacts, which arise when signals originating in tissue appear in contrast agent-specific imaging mode. In addition, the B-mode ultrasound image used for anatomy is less diagnostically useful than, for example, the computed tomography (CT) image in combined positron emission tomography-computed tomography (PET/CT) or single photon emission computed tomography-computed tomography (SPECT/CT) systems. These multi-modality systems allow the molecular scan to be overlaid onto a CT scan, enabling spatial localization of targeting, and have demonstrated higher accuracy in localizing tumors of the lung, thyroid, breast, and prostate relative to molecular imaging alone [6–11]. In some cases, combined SPECT and CT angiography images have been used to visualize molecular targeting relative to hemodynamics, either using an integrated system [12] or in sequentially-acquired images [13]. By combining molecular images with angiographic rather than tissue data, these systems contribute unique diagnostic information not found in typical SPECT/CT images.

While ultrasound molecular imaging has been utilized widely in preclinical imaging studies, until recently there were obstacles to the use of targeted microbubbles in humans because targeted microbubbles were frequently formulated with streptavidin in the shell, which produces an immune response in humans [14]. Recently, several advancements have been made towards imaging in humans, including the development of a phospholipid-shelled microbubble with a lipopeptide targeted to vascular endothelial growth factor receptor 2 (VEGFR2) [15], a single-chain VEGF microbubble [16], a Cyclo-Arg-Gly-Asp-D-Tyr-Cys (cyclic RGD) microbubble targeted to the $\alpha_v\beta_3$ integrin [17], a protein-shelled multi-modal agent targeted to $\alpha_v\beta_3$ [18], and a lipid-shelled microbubble targeted to E-selectin [19]. Researchers have also recently presented a polymer-shelled microbubble targeted to E-selectin that can be imaged at very low doses, potentially mitigating the immune response [20].

Ultrasound molecular images are typically overlaid on a grayscale B-mode ultrasound image, a map indicating differential acoustic impedance of tissue scatterers—typically many randomly-positioned sub-resolution scatterers that produce constructive interference, or speckle [21]. In ultrasound, the molecular image that is overlaid onto the B-mode image is typically formed using contrast-specific multi-pulse sequences, which cancel the linear signals produced by tissue and form images using only the nonlinear signals, ideally microbubbles alone [22]. In reality, nonlinear (i.e. harmonic) signals are produced by many structures in tissue [23], causing high-amplitude tissue artifacts in microbubble-specific imaging techniques [24, 25], which reduces contrast-to-tissue ratio (CTR) and can make images more difficult to interpret. An alternative approach for contrast-specific ultrasound imaging is superharmonic imaging, which requires a non-traditional ultra-wide-band transducer (often designed with two separate low and high frequency transmit and receive elements) to receive signals produced by microbubbles at frequencies many times higher than the transmitted frequency, where tissue harmonics are extremely low in amplitude [26, 27]. We have previously demonstrated the application of superharmonic detection for imaging 3-D volumes of tissue [28]. This technique produces high resolution, high contrast-to-tissue images of the microvasculature, and hence is referred to as “acoustic angiography” because the images resemble traditional x-ray angiography. This method has recently been used to identify developing tumors as small as 2–3 mm on the basis of detecting a tumor’s angiogenic fingerprint from image-derived metrics of vessel tortuosity [29], and to illustrate that vascular remodeling occurs outside of the tumor itself [30]. Using this technique, CTRs as high as 25.5 dB have been measured *in vitro* [31]. *In vivo* CTR may be improved by adjusting the shape of the transmitted acoustic pulse to further reduce tissue artifact [32]. Using a prototype dual-frequency transducer [28], the resolution of this approach in vascular imaging is ~100 μm, although the presence of microbubbles in sub-resolution vessels can also be detected and quantified [33].

Despite its ability to form high resolution, high contrast vascular images, acoustic angiography is a challenging tool to use for molecular imaging because the superharmonic signals are associated with substantial microbubble oscillations which often lead to microbubble shell rupture and gas dissolution over one or multiple pulses [34]. However, it is possible to perform acoustic angiography with the same bubbles repeatedly through reduced acoustic pressures and minimized bubble acoustic exposure with low frame rates. By controlling the transmitted acoustic pressure and the step size between successive transmit pulses, we have previously demonstrated the ability to form high resolution, high contrast superharmonic molecular images which can be overlaid on microvascular images [35]. These imaging volumes might be useful for treatment planning and monitoring in highly vascularized tumors. In this work, we describe the use of this high resolution approach, molecular acoustic angiography, to image fibrosarcoma tumors in rodents. The purpose of this study is to measure the CTR and analyze the response to varying microbubble dose for both superharmonic and multi-pulse ultrasound molecular imaging and to assess the ability to analyze spatial relationships between molecular and microvascular imaging volumes in vascular tumors.

Material and Methods

Animal imaging

The Fisher 344 rat fibrosarcoma (FSA) model was prepared as previously described, with a ~1 mm-sized piece of tumor implanted subcutaneously in the flank of 14 animals [36]. *In vivo* imaging began on the eighth day after tumor implantation when tumors were 5.9 ± 1.6 mm in diameter. Imaging was performed under anesthesia via vaporized isoflurane and oxygen; contrast agents were injected using a 24 gauge catheter inserted into a tail vein. Fur was removed by shaving and depilation, and ultrasound gel was applied to the skin. A heated imaging stage was used to maintain body temperature. Acquisition times were less than 1 min for each B-mode or molecular volume and between 1 and 2 min for each microvascular volume. All animal experiments were performed in accordance with the Institutional Animal Care and Use Committee of The University of North Carolina at Chapel Hill.

The image acquisition workflow is illustrated in Fig. 1. Each animal was first imaged using a Siemens Sequoia 512 (Mountain View, CA) and a 15L8 linear array transducer. The transducer was mounted on a linear motion stage to acquire 3D volumes with a step size of 250 μm. A B-mode volume was acquired, followed by a contrast-specific pre-scan volume. Next, a bolus of microbubbles targeted to VEGFR2 (single chain, Targeson Visistar® VEGFR2, San Diego, CA) was injected. After a 12 min wait for free bubbles to clear, targeted images were acquired in contrast-specific imaging mode. All microbubbles were then destroyed using the motion stage to translate the transducer through the imaging region while transmitting a high-mechanical index pulse (MI=1.9). Finally, a post-destruction imaging volume was acquired for comparison. Contrast-specific images were acquired using multi-pulse contrast pulse sequence (CPS) mode [22] at a frequency of 3.5/7 MHz and a mechanical index of 0.18. B-mode images were acquired using the same transducer at 14 MHz and a mechanical index of 0.72.

The animal was then imaged using a modified VisualSonics Vevo 770 system with a prototype transducer [28] for molecular acoustic angiography. This mechanically-steered transducer transmits at 4 MHz and receives at 30 MHz. It is also mounted on a motion stage for acquisition of 3D volumes. Animal preparation was identical to that previously described. For acoustic angiography scans, most artifacts such as shadowing or high-amplitude tissue artifacts can be avoided by adequate depilation and gel application, just as in general small animal imaging with ultrasound. Again, a B-mode (30 MHz) imaging volume was acquired, followed by a dual-frequency (transmit 4 MHz/receive 30 MHz, MI = 0.62) pre-scan, followed by injection of a bolus of VEGFR2-targeted microbubbles. After a 12 min wait, targeted images were acquired using a step size of 250 μm to ensure microbubbles were not destroyed when imaging the adjacent imaging plane [35]. Three more 3D scans were performed at an MI of 0.62 to ensure all bound microbubbles were destroyed before acquisition of a post-destruction volume. Destruction of targeted microbubbles was confirmed visually and by comparison of pre-scan and post-destruction images. Finally, an infusion of 1.5×10^8 untargeted microbubbles/min was injected using a pump (Harvard Apparatus, PHD2000) and microvascular imaging volumes were acquired

with a step size of 100 μm between 2D images. 14 animals were scanned using this protocol for three consecutive days.

Prior to microvascular imaging, 5 of 14 animals received a single additional bolus injection of microbubbles targeted to both E- and P-selectin (Targeson Visistar® Selectin, San Diego, CA). The use of a second targeted microbubble with a different targeting moiety allows comparison between microvascular morphology with molecular information in both VEGFR2 (angiogenesis) and selectin (inflammation) imaging volumes. Tumor-specific binding of microbubbles targeted to inflammatory markers E- and P-selectin has previously been observed by other researchers [37, 38]. The upregulation of P- and E-selectin expression during tumor growth and metastasis [39–44] has previously been reported, as VEGFR2 enhances E-selectin induction in association with tumor necrosis factor α (TNF-α) [45].

Microbubble dose

Three bolus doses of VEGFR2-targeted microbubbles were used: 7.6×10^6, 1.25×10^7, and 2.5×10^7 microbubbles, determined using an Accusizer 780 (Particle Sizing Systems, Santa Barbara, CA). Each animal was randomly assigned one of the three doses on day 1, then rotated through the other two doses on days 2 and 3 so that every animal received each dose in random order. Imaging was always performed first using conventional multi-pulse imaging (Siemens CPS), thus any effects due to multiple injections (i.e. targeting locations being blocked due to the first injection of VEGFR2-targeted bubbles) would appear only on the molecular acoustic angiography scan and would be identical for all animals. Animals receiving a second bolus of microbubbles targeted to E- and P-selectin received a dose matched to the dose of VEGF-targeted microbubbles they received that day (either 7.6×10^6 or 2.5×10^7 microbubbles/ml).

Image processing and analysis

For molecular imaging data acquired using VEGFR2-targeted microbubbles and multi-pulse imaging (Siemens CPS), the region containing the tumor was determined by manually drawing a 2D region of interest (ROI) around the tumor (CPS mode images, Fig. 1b, bottom row) using a custom program (Matlab, The Mathworks, Natick, MA). ROIs were drawn in each imaging slice containing a tumor for every animal. The mean value of the image intensity within each ROI in the targeted imaging volumes was computed, and microbubble signal from any remaining free-flowing bubbles was accounted for by subtracting the mean intensity of the post-destruction frames for the same ROI. In order to compute image intensity from tissue, the manually-selected ROI was laterally translated to three other locations adjacent to the tumor and were separated by a distance greater than the lateral dimension of the tumor. Computation of tissue signal was performed using pre-scans that did not contain microbubbles. The mean of all three regions in all tumor-containing slices was computed. Image intensity is typically used to quantify contrast signal in ultrasound molecular imaging even though this signal has undergone compression before being displayed, which may result in nonlinear mapping of signal amplitudes.

For molecular imaging data acquired using VEGFR2-targeted microbubbles and dual-frequency superharmonic imaging (molecular acoustic angiography), the tumor-containing region was determined by manually drawing ROIs around the image in each 2D slice (Fig. 1b, top row) containing a tumor in the VEGFR2-targeted volume using a custom Matlab program, and the ROI was applied to the post-destruction volume to calculate mean signal from any remaining microbubbles in circulation. To compute the image intensity from tissue, the ROI was again laterally translated to three other locations adjacent to the tumor and were separated by a distance greater than the lateral dimension of the tumor. Tissue computations were made using pre-scans that did not contain microbubbles.

Mean intensity of pre-injection and post-destruction images were compared using t-tests for both multi-pulse imaging and superharmonic imaging and no significant differences were found, indicating that targeted images were not significantly influenced by free bubbles remaining in circulation after the 12 min wait. Microbubble dose groups were analyzed using ANOVA and Tukey post-hoc analysis to compare targeting signal intensity for each of the 3 microbubble doses tested using both imaging techniques.

For microvascular imaging data acquired using non-targeted microbubbles and dual-frequency superharmonic imaging (acoustic angiography), tumor regions were masked using the manually-drawn ROIs, and individual tumor vessels (e.g. those seen in Fig. 1e, top row) were segmented from the imaging volumes using centerline extraction via height ridge traversal with manually defined seed points [46]. Coordinates of the centroid of molecular imaging targeting sites were determined using a custom Matlab program. These targeting site coordinates and coordinates from vessel segmentations were read into Matlab. Vessel coordinates were down-sampled to match the image spacing of the molecular imaging data. For each vessel in a segmented microvascular volume, the distance from every point on this vessel to every targeting site was determined. Vessel diameter, as determined by the segmentation process, was accounted for in computing this distance. Finally, vessel tortuosity was computed [46, 47] and related to the distance between individual vessels and molecular targeting sites.

Results

Comparison of multi-pulse and superharmonic molecular imaging

Typical images before and after injection of VEGFR2-targeted microbubbles for both multi-pulse and superharmonic imaging approaches are shown in Fig. 2 for an example microbubble dose. On-screen intensities were used to evaluate targeting, as is customary in ultrasound molecular imaging. However, unlike most ultrasound molecular imaging systems, the superharmonic molecular imaging volume contains many dark regions punctuated by bright targeting sites due to its high resolution (Fig. 2). Thus ROIs in superharmonic images contain many near-zero values, causing averaging over an ROI to depress the mean.

Analysis using ANOVA revealed that targeting intensity for both imaging techniques varies with contrast dose ($p = 9 \times 10^{-7}$ for multi-pulse, $p = 1 \times 10^{-3}$ for superharmonic). Tukey post-hoc analysis further showed that neither technique detected a significant difference in targeting between the lowest microbubble dose (7.6×10^{6}) and the intermediate dose (1.25 ×

10^7). However, the highest contrast dose tested (2.5×10^7) resulted in significantly greater targeting signal intensity for both imaging techniques ($p < 0.01$). Contrast-to-tissue ratio (CTR) was computed for each imaging approach using the ROIs drawn in the tissue-containing regions in the pre-scans and the tumor-containing regions in the targeted images. By normalizing to tissue signals, system-dependent differences are greatly reduced. CTR grouped by dose for all administrations of VEGFR2-targeted microbubbles in 14 animals is shown in Fig. 3. Mean CTR was 0.53 dB for multi-pulse molecular imaging (Siemens Sequoia CPS mode) and 13.98 dB for superharmonic molecular imaging ($p = 4.9 \times 10^{-10}$).

Spatial analysis of microvascular and molecular acoustic angiography imaging

Illustrative co-registered acoustic angiography images of microvasculature and molecular imaging are displayed in Fig. 4. The images shown are maximum intensity projections of microvascular and molecular imaging volumes acquired sequentially in one of the five animals receiving sequential injections of VEGFR2- and selectin-targeted microbubbles.

Segmented images containing only tumor vasculature are displayed in Fig. 5. After segmentation, each “tube” representing a vessel is described by centerline coordinates and a radius at each point along its length (Fig. 5a). The segmented centerlines are used to compute vessel tortuosity, which can be displayed as a color-coded map of tortuosity on the vasculature (Fig. 5b). Targeting sites from either co-registered VEGFR2 (Fig. 5c) or selectin (Fig. 5d) molecular imaging can be overlaid on a tortuosity map. While it is challenging to visualize precise spatial relationships between vessel tortuosity and targeting in this 2D display format, Fig. 5 allows for conceptualization of the acquired data sets, which have been parameterized to a 3D data set consisting of local vessel tortuosity and intra-tumoral targeting of two different contrast agents.

Mean tortuosity (distance metric [47]) is displayed as a function of distance to the targeting site in Fig. 6. Both VEGFR2 and selectin-targeted microbubbles exhibit decreases in tortuosity over distances of 100s of micrometers. The trends are similar across the two different types of agents, with maximum tortuosity values occurring very close to both VEGFR2 and selectin-targeting locations.

Discussion

Comparison of multi-pulse and superharmonic molecular imaging

Although differences between doses on the basis of on-screen image intensity were only statistically significant for the largest microbubble dose, superharmonic molecular imaging showed increased tissue rejection and increased separation between dose groups relative to multi-pulse imaging. As mentioned, analysis of molecular imaging using the standard approach based on image intensity is difficult given the large number of near-zero values in the superharmonic molecular imaging volume (Fig. 2). Because of this and the excellent ability of superharmonic imaging to reject tissue, computed CTR values are much higher for superharmonic than for multi-pulse molecular imaging (13.98 dB vs. 0.53 dB; $p = 4.9 \times 10^{-10}$).

We previously reported that the molecular superharmonic signal decreases by ~50% from the first to the second scan, and nearly to the noise floor after the third scan, indicating that most microbubbles are destroyed rapidly by this process [35]. However, it is unclear how many bubbles might be destroyed or dislodged by off-axis acoustic pressure on a given microbubble when the beam is in a prior imaging location. Thus there may be more targeted bubbles present, and the targeting may be less sparse than what can be imaged using the current imaging system and prototype transducer.

Spatial analysis of microvascular and molecular acoustic angiography imaging

In addition to the improved CTR of the superharmonic contrast imaging approach, another advantage of this technology is the ability to combine molecular imaging with the vascular morphology information provided by acoustic angiography. We have demonstrated the feasibility of quantitative spatial analysis of vessel tortuosity and molecular targeting for the first time (Fig. 6). Differences in tortuosity as a function of distance from individual targeting sites were observed at very small distances (inter-group step sizes ≤ 100 μm) while still within the tumor itself. This complements our previous work, which indicates that changes in vessel tortuosity occur outside of the margins of solid tumors [30]. In this study, tortuosity within the tumor was observed to decrease with distance from VEGFR2 and selectin targeting locations, suggesting a relationship between both endothelial biomarkers and the tortuous morphology arising in the dysfunctional tumor microenvironment. While VEGF is the most prominent molecule associated with angiogenesis in the literature [48–50], selectin-targeted microbubbles have previously been reported to produce a higher targeting signal than VEGFR2-targeted bubbles in a murine model of colon adenocarcinoma, particularly for small tumors [51]. There is also evidence that VEGF plays an important role in regulating expression of E-selectin [45, 52] and that selectins are involved in angiogenesis, independently of VEGF [53–57]. Specifically, previous studies have shown that anti-E-selectin antibodies inhibit capillary tube formation *in vitro* [57], and that exogenous E-selectin induces angiogenesis *in vivo* in the rat cornea [54]. In addition, in investigating the role of P-selectin in angiogenesis in a hind-limb ischemia model, researchers found that P-selectin knockout mice exhibited significantly lower capillary density, as fewer leukocytes infiltrated into ischemic tissues and fewer of the infiltrated leukocytes expressed VEGF [53].

The similar trends in tortuosity with distance for both agents may also reflect microbubble kinetics in small angiogenic vessels, which tend to have low shear flow, with binding efficiency in shear flow also dependent upon ligand concentration on the microbubble surface [58, 59]. While shear flow is a major determining factor in flow kinetics [60], increased shear stress is also correlated with reduced E-selectin expression [61, 62], consistent with high E-selectin expression in tumor angiogenesis.

Microbubble oscillation has been reported to decrease in smaller vessels [63], i.e. the newly-formed and tortuous vessels found in tumor angiogenesis [64]. It is unknown exactly how this physical confinement effect translates to superharmonic imaging, though we have previously observed that transitioning from *in vitro* to *in vivo* experiments in vessels of the same diameters required scaling of acoustic pressures by factors greater than what can be

explained by attenuation [35]. Superharmonic molecular imaging also requires higher peak acoustic pressures than multi-pulse techniques [34].

Conclusions

Superharmonic molecular imaging, or molecular acoustic angiography, exhibits a significant increase in CTR relative to traditional ultrasound molecular imaging techniques. Due to the high resolution of acoustic angiography molecular imaging, it is possible to co-relate microvascular and molecular information contained in ultrasound superharmonic imaging volumes. This allows for direct comparison between geometry of newly-forming tumor vasculature and the markers expressed by endothelial cells within the tumor. In order to better understand and analyze these relationships, future studies are required to separate the effects of binding efficiency and blood flow kinetics.

Acknowledgments

This work was supported by grants R01CA170665, R01CA189479, U01CA189281, F32EB018715, and T32HL069768 from the National Institutes of Health. We thank Mike Lee and Emmanuel Cherin for their contributions to the design and fabrication of prototype transducers. Animal Studies were performed within the Lineberger Comprehensive Cancer Center (LCCC) Animal Studies Core Facility at the University of North Carolina at Chapel Hill. The LCCC Animal Studies Core is supported in part by an NCI Center Core Support Grant (CA16086) to the UNC Lineberger Comprehensive Cancer Center.

F. Stuart Foster is a consultant and receives research funding from VisualSonics, Inc. F. Stuart Foster and Paul A. Dayton are inventors on a pending patent describing the acoustic angiography technology. Paul A. Dayton is a co-founder of SonoVol, Inc., a company which has licensed the patent enabling acoustic angiography.

References

1. Dayton PA, Ferrara KW. Targeted imaging using ultrasound. Journal of magnetic resonance imaging : J Mang Res Imaging. 2002; 16:362–77.
2. Gessner R, Dayton PA. Advances in molecular imaging with ultrasound. Mol Imaging. 2010; 9:117–27. [PubMed: 20487678]
3. Villanueva FS, Jankowski RJ, Manaugh C, et al. Albumin microbubble adherence to human coronary endothelium: Implications for assessment of endothelial function using myocardial contrast echocardiography. J Am Coll Cardiol. 1997; 30:689–693. [PubMed: 9283527]
4. Lindner JR, Coggins MP, Kaul S, et al. Microbubble persistence in the microcirculation during ischemia/reperfusion and inflammation is caused by integrin- and complement-mediated adherence to activated leukocytes. Circulation. 2000; 101:668–675. [PubMed: 10673260]
5. Ferrara KW, Borden MA, Zhang H. Lipid-shelled vehicles: engineering for ultrasound molecular imaging and drug delivery. Accounts Chem Res. 2009; 42:881–92.
6. Roach PJ, Schembri GP, Shon IAH, et al. SPECT/CT imaging using a spiral CT scanner for anatomical localization: Impact on diagnostic accuracy and reporter confidence in clinical practice. Nucl Med Commun. 2006; 27:977–987. [PubMed: 17088684]
7. Cerfolio RJ, Ojha B, Bryant AS, et al. The accuracy of integrated PET-CT compared with dedicated PET alone for the staging of patients with nonsmall cell lung cancer. Ann Thorac Surg. 2004; 78:1017–23. [PubMed: 15337041]
8. Tharp K, Israel O, Hausmann J, et al. Impact of I-131-SPECT/CT images obtained with an integrated system in the follow-up of patients with thyroid carcinoma. Eur J Nucl Med Mol Imaging. 2004; 31:1435–1442. [PubMed: 15221294]
9. Lerman H, Lievshitz G, Zak O, et al. Improved sentinel node identification by SPECT/CT in overweight patients with breast cancer. J Nucl Med. 2007; 48:201–206. [PubMed: 17268015]

10. Garami Z, Hascsi Z, Varga J, et al. The value of 18-FDG PET/CT in early-stage breast cancer compared to traditional diagnostic modalities with an emphasis on changes in disease stage designation and treatment plan. Eur J Surg Oncol. 2012; 38:31–7. [PubMed: 21937190]
11. Soyka JD, Muster MA, Schmid DT, et al. Clinical impact of 18F-choline PET/CT in patients with recurrent prostate cancer. Eur J Nucl Med Mol Imaging. 2012; 39:936–43. [PubMed: 22415598]
12. Rispler S, Keidar Z, Ghersin E, et al. Integrated single-photon emission computed tomography and computed tomography coronary angiography for the assessment of hemodynamically significant coronary artery lesions. J Am Coll Cardiol. 2007; 49:1059–67. [PubMed: 17349885]
13. Grani C, Benz DC, Schmied C, et al. Hybrid CCTA/SPECT myocardial perfusion imaging findings in patients with anomalous origin of coronary arteries from the opposite sinus and suspected concomitant coronary artery disease. J Nucl Cardiol. 2015; doi: 10.1007/s12350-015-0342
14. Meyer DL, Schultz J, Lin YK, et al. Reduced antibody response to streptavidin through site-directed mutagenesis. Protein Sci. 2001; 10:491–503. [PubMed: 11344318]
15. Pochon S, Tardy I, Bussat P, et al. BR55: a lipopeptide-based VEGFR2-targeted ultrasound contrast agent for molecular imaging of angiogenesis. Invest Radiol. 2010; 45:89–95. [PubMed: 20027118]
16. Anderson CR, Rychak JJ, Backer M, et al. scVEGF microbubble ultrasound contrast agents: a novel probe for ultrasound molecular imaging of tumor angiogenesis. Invest Radiol. 2010; 45:579–85. [PubMed: 20733505]
17. Anderson CR, Hu X, Zhang H, et al. Ultrasound molecular imaging of tumor angiogenesis with an integrin targeted microbubble contrast agent. Invest Radiol. 2011; 46:215–24. [PubMed: 21343825]
18. John R, Nguyen FT, Kolbeck KJ, et al. Targeted Multifunctional Multimodal Protein-Shell Microspheres as Cancer Imaging Contrast Agents. Mol Imaging Biol. 2012; 14:17–24. [PubMed: 21298354]
19. Yeh JS, Sennoga CA, McConnell E, et al. A Targeting Microbubble for Ultrasound Molecular Imaging. PloS one. 2015; 10:e0129681. [PubMed: 26161541]
20. Spivak I, Rix A, Schmitz G, et al. Low-Dose Molecular Ultrasound Imaging with E-Selectin-Targeted PBCA Microbubbles. Mol Imaging Biol. 2016; 18:180–90. [PubMed: 26391990]
21. Wagner RF, Smith SW, Sandrik JM, et al. Statistics of Speckle in Ultrasound B-Scans. IEEE T Son Ultrason. 1983; 30:156–163.
22. Phillips, P. IEEE Ultrasonics Symposium; 2001. p. 1739-1745.
23. Christopher T. Finite amplitude distortion-based inhomogeneous pulse echo ultrasonic imaging. IEEE T Syst Man Cy C. 1997; 44:125–39.
24. Yildiz YO, Eckersley RJ, Senior R, et al. Correction of Non-Linear Propagation Artifact in Contrast-Enhanced Ultrasound Imaging of Carotid Arteries: Methods in In Vitro Evaluation. Ultrasound Med Biol. 2015; 41:1938–47. [PubMed: 25935597]
25. Herbst, EB., Unnikrishnan, S., Wang, SY., et al. The Use of Acoustic Radiation Force Decorrelation Weighted Pulse Inversion (ADW-PI) in Enhancing Microbubble Contrast; 2015 IEEE International Ultrasonics Symposium (IUS); 2015.
26. Bouakaz A, Krenning BJ, Vletter WB, et al. Contrast superharmonic imaging: a feasibility study. Ultrasound Med Biol. 2003; 29:547–53. [PubMed: 12749924]
27. Kruse DE, Ferrara KW. A new imaging strategy using wideband transient response of ultrasound contrast agents. IEEE T Ultrason Ferr. 2005; 52:1320–1329.
28. Gessner R, Lukacs M, Lee M, et al. High-resolution, high-contrast ultrasound imaging using a prototype dual-frequency transducer: in vitro and in vivo studies. IEEE T Syst Man Cy C. 2010; 57:1772–81.
29. Shelton SE, Lee YZ, Foster FS, et al. Quantification of microvascular tortuosity during tumor evolution utilizing acoustic angiography. Ultrasound Med Biol. 2015; 41:1896–1904. [PubMed: 25858001]
30. Rao S, Shelton S, Dayton P. The 'fingerprint' of cancer extends beyond solid tumor boundaries: assessment with a novel ultrasound imaging approach. IEEE T Bio-Med Eng. 2016; 63:1082–1086.

31. Lindsey BD, Rojas JD, Martin KH, et al. Acoustic characterization of contrast-to-tissue ratio and axial resolution for dual-frequency contrast-specific acoustic angiography imaging. IEEE T Syst Man Cy C. 2014; 61:1668–87.
32. Lindsey BD, Shelton SE, Dayton PA. Optimization of contrast-to-tissue ratio through pulse windowing in dual-frequency "acoustic angiography" imaging. Ultrasound Med Biol. 2015; 41:1884–95. [PubMed: 25819467]
33. Dunleavey JM, Xiao L, Thompson J, et al. Vascular channels formed by subpopulations of PECAM1+ melanoma cells. Nature Commun. 2014; 5:5200. [PubMed: 25335460]
34. Lindsey BD, Rojas JD, Dayton PA. On the relationship between microbubble fragmentation, deflation, and broadband superharmonic signal production. Ultrasound Med Biol. 2015; 41:1711–1725. [PubMed: 25766572]
35. Shelton SE, Lindsey BD, Tsuruta JK, et al. Molecular acoustic angiography: a new technique for high resolution superharmonic ultrasound molecular imaging. Ultrasound Med Biol. 2016; 42:769–781. [PubMed: 26678155]
36. Yuan H, Schroeder T, Bowsher JE, et al. Intertumoral differences in hypoxia selectivity of the PET imaging agent 64Cu(II)-diacetyl-bis(N4-methylthiosemicarbazone). J Nucl Med. 2006; 47:989–98. [PubMed: 16741309]
37. Fokong S, Fragoso A, Rix A, et al. Ultrasound Molecular Imaging of E-Selectin in Tumor Vessels Using Poly n-Butyl Cyanoacrylate Microbubbles Covalently Coupled to a Short Targeting Peptide. Invest Radiol. 2013; 48:843–850. [PubMed: 23857137]
38. Warram JM, Sorace AG, Mahoney M, et al. Biodistribution of P-selectin targeted microbubbles. J Drug Target. 2014; 22:387–94. [PubMed: 24731055]
39. Biancone L, Araki M, Araki K, et al. Redirection of tumor metastasis by expression of E-selectin in vivo. J Exp Med. 1996; 183:581–587. [PubMed: 8627169]
40. Caine GJ, Lip GY, Blann AD. Platelet-derived VEGF, Flt-1, angiopoietin-1 and P-selectin in breast and prostate cancer: further evidence for a role of platelets in tumour angiogenesis. Annal Med. 2004; 36:273–7.
41. Caine GJ, Lip GY, Stonelake PS, et al. Platelet activation, coagulation and angiogenesis in breast and prostate carcinoma. Thromb Haemost. 2004; 92:185–90. [PubMed: 15213860]
42. Blann AD, Gurney D, Wadley M, et al. Increased soluble P-selectin in patients with haematological and breast cancer: a comparison with fibrinogen, plasminogen activator inhibitor and von Willebrand factor. Blood Coag Fibrin. 2001; 12:43–50.
43. Schadendorf D, Diehl S, Zuberbier T, et al. Quantitative detection of soluble adhesion molecules in sera of melanoma patients correlates with clinical stage. Dermatology. 1996; 192:89–93. [PubMed: 8829517]
44. Haznedaroglu IC, Benekli M, Ozcebe O, et al. Serum L-selectin and P-selectin levels in lymphomas. Haematologia. 2000; 30:27–30. [PubMed: 10841321]
45. Stannard AK, Khurana R, Evans IM, et al. Vascular endothelial growth factor synergistically enhances induction of E-selectin by tumor necrosis factor-alpha. Arterioscl Thromb Vasc Biol. 2007; 27:494–502. [PubMed: 17170373]
46. Aylward SR, Bullitt E. Initialization, noise, singularities, and scale in height ridge traversal for tubular object centerline extraction. IEEE Trans Med Imaging. 2002; 21:61–75. [PubMed: 11929106]
47. Bullitt E, Muller KE, Jung I, et al. Analyzing attributes of vessel populations. Medical Image Anal. 2005; 9:39–49.
48. Dvorak HF. Tumors: Wounds That Do Not Heal- Redux. Cancer Immunol Res. 2015; 3:1–11. [PubMed: 25568067]
49. Ferrara N, Gerber HP, LeCouter J. The biology of VEGF and its receptors. Nature medicine. 2003; 9:669–76.
50. Carmeliet P. VEGF as a key mediator of angiogenesis in cancer. Oncology. 2005; 69(Suppl 3):4–10. [PubMed: 16301830]
51. van Wamel A, Celebi M, Hossack JA, et al. Molecular imaging with targeted contrast agents and high frequency ultrasound. 2007 Ieee Ultrasonics Symposium Proceedings. 2007; 1–6:961–964.

52. Aoki M, Kanamori M, Yudoh K, et al. Effects of vascular endothelial growth factor and E-selectin on angiogenesis in the murine metastatic RCT sarcoma. Tumour biology Journal Int Soc Oncodevelop Biol Med. 2001; 22:239–46.

53. Egami K, Murohara T, Aoki M, et al. Ischemia-induced angiogenesis: role of inflammatory response mediated by P-selectin. J Leukocyte Biol. 2006; 79:971–6. [PubMed: 16641139]

54. Koch AE, Halloran MM, Haskell CJ, et al. Angiogenesis mediated by soluble forms of E-selectin and vascular cell adhesion molecule-1. Nature. 1995; 376:517–9. [PubMed: 7543654]

55. Oh IY, Yoon CH, Hur J, et al. Involvement of E-selectin in recruitment of endothelial progenitor cells and angiogenesis in ischemic muscle. Blood. 2007; 110:3891–9. [PubMed: 17699745]

56. Nishiwaki Y, Yoshida M, Iwaguro H, et al. Endothelial E-selectin potentiates neovascularization via endothelial progenitor cell-dependent and -independent mechanisms. Arterioscl Thromb Vasc Biol. 2007; 27:512–8. [PubMed: 17170379]

57. Nguyen M, Folkman J, Bischoff J. 1-Deoxymannojirimycin inhibits capillary tube formation in vitro. Analysis of N-linked oligosaccharides in bovine capillary endothelial cells. J Biol Chem. 1992; 267:26157–65. [PubMed: 1464626]

58. Klibanov AL, Rychak JJ, Yang WC, et al. Targeted ultrasound contrast agent for molecular imaging of inflammation in high-shear flow. Contrast Media Mol imaging. 2006; 1:259–66. [PubMed: 17191766]

59. Patil AV, Rychak JJ, Klibanov AL, et al. Real-time technique for improving molecular imaging and guiding drug delivery in large blood vessels: in vitro and ex vivo results. Mol Imaging. 2011; 10:238–47. [PubMed: 21521555]

60. Takalkar AM, Klibanov AL, Rychak JJ, et al. Binding and detachment dynamics of microbubbles targeted to P-selectin under controlled shear flow. J Controlled Release. 2004; 96:473–82.

61. Chiu JJ, Lee PL, Chen CN, et al. Shear stress increases ICAM-1 and decreases VCAM-1 and E-selectin expressions induced by tumor necrosis factor-alpha in endothelial cells. Arterioscl Throm Vas. 2004; 24:73–79.

62. Dimitroff CJ, Lechpammer M, Long-Woodward D, et al. Rolling of human bone-metastatic prostate tumor cells on human bone marrow endothelium under shear flow is mediated by E-selectin. Cancer Res. 2004; 64:5261–5269. [PubMed: 15289332]

63. Caskey CF, Stieger SM, Qin S, et al. Direct observations of ultrasound microbubble contrast agent interaction with the microvessel wall. J Acoust Soc Am. 2007; 122:1191–1200. [PubMed: 17672665]

64. Li CY, Shan S, Huang Q, et al. Initial stages of tumor cell-induced angiogenesis: evaluation via skin window chambers in rodent models. J Natl Cancer Inst. 2000; 92:143–7. [PubMed: 10639516]

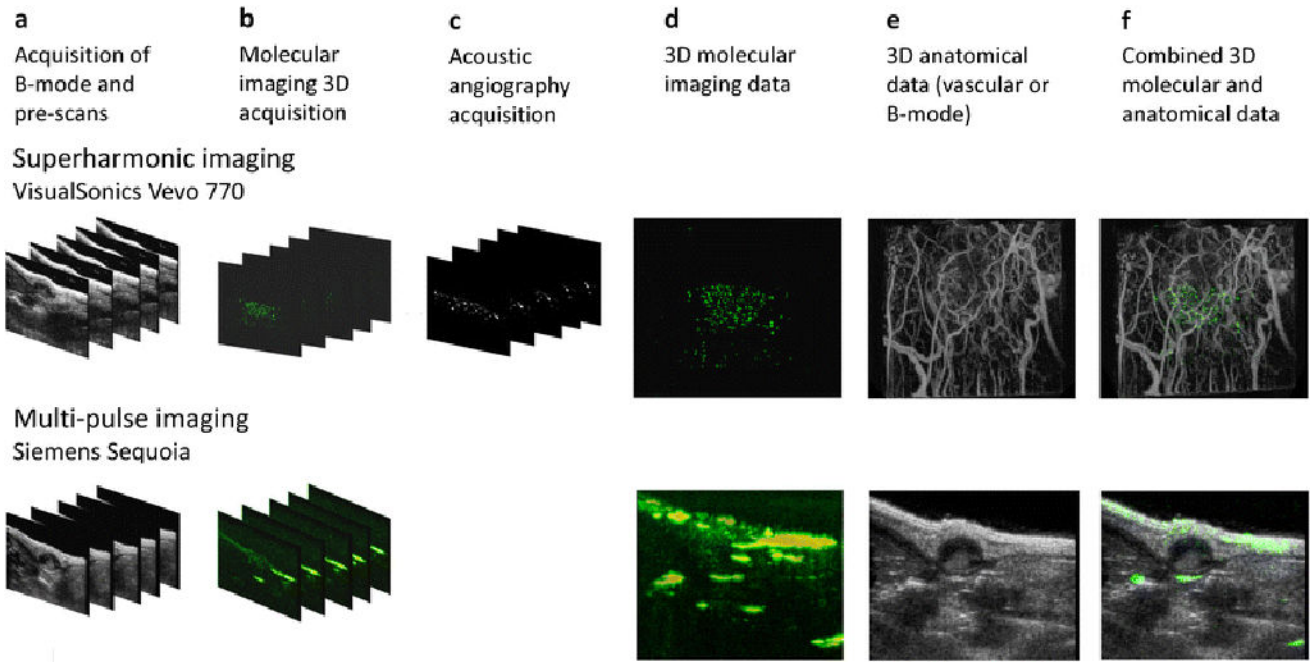

Fig. 1.

Data acquisition and image processing flow for both superharmonic (acoustic angiography; top row) and multi-pulse (bottom row) ultrasound molecular imaging. All animals were imaged using both systems on the same day. **a** 3D B-mode and contrast-specific pre-scans are acquired using a motorized motion stage. **b** Targeted contrast agent is administered and 3D images are acquired in contrast-specific imaging modes after a 12 min wait. Targeted bubbles are then destroyed by high MI scanning, and a post-scan is acquired. **c** Free microbubbles are administered and a microvascular imaging or “acoustic angiography” scan is acquired for the superharmonic imaging case only. Using the described data sets, it is now possible to combine **d** 3D molecular imaging data sets on both systems, with **e** either vascular or B-mode data to produce **f** combined visualizations of anatomical and functional imaging data.

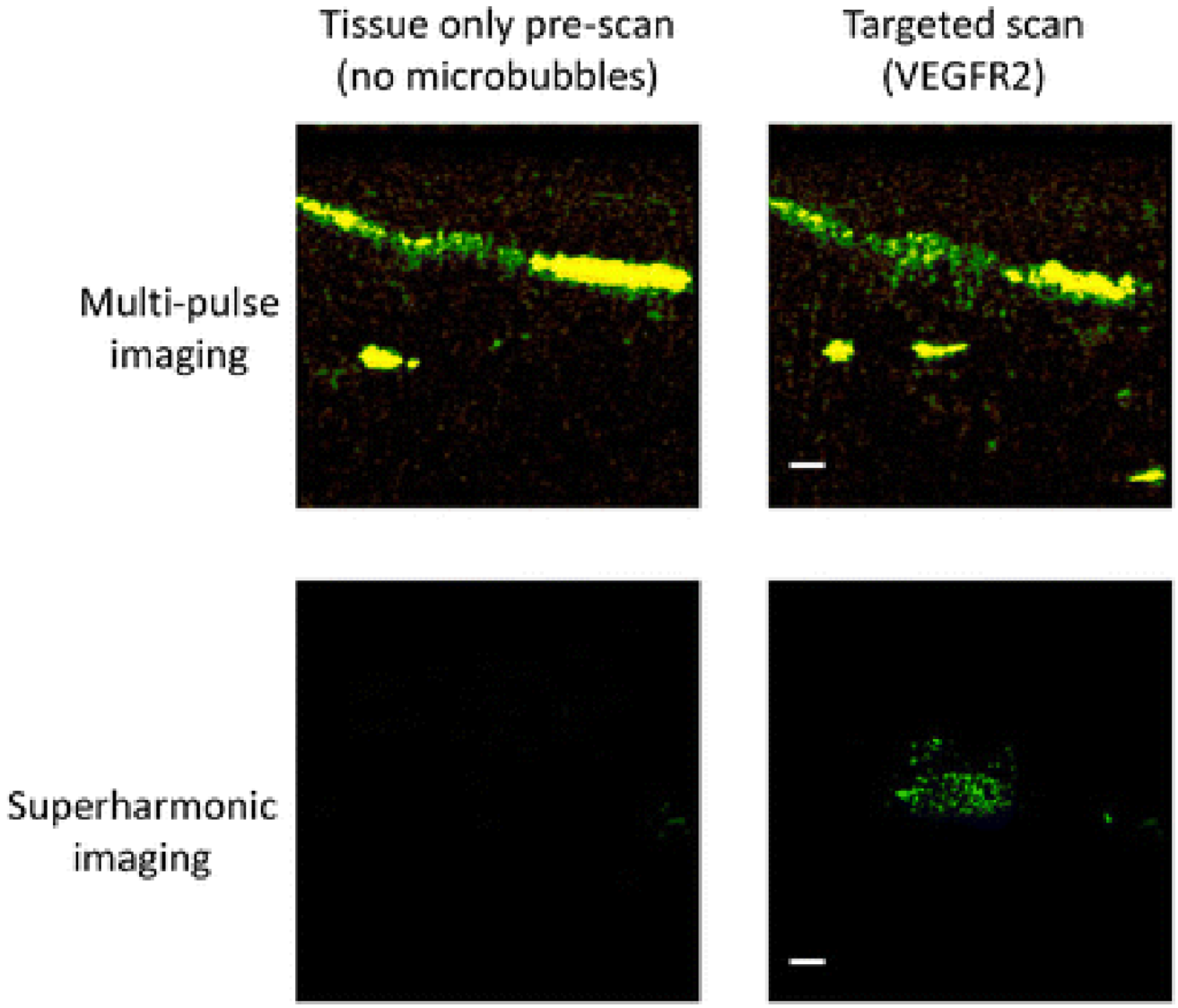

Fig. 2.

Illustrative images for the cases shown in Fig 1 demonstrate the tissue-only images before a bolus injection of 1.25×10^6 microbubbles for both multi-pulse and superharmonic ultrasound molecular imaging. Scale bars represent 2 mm.

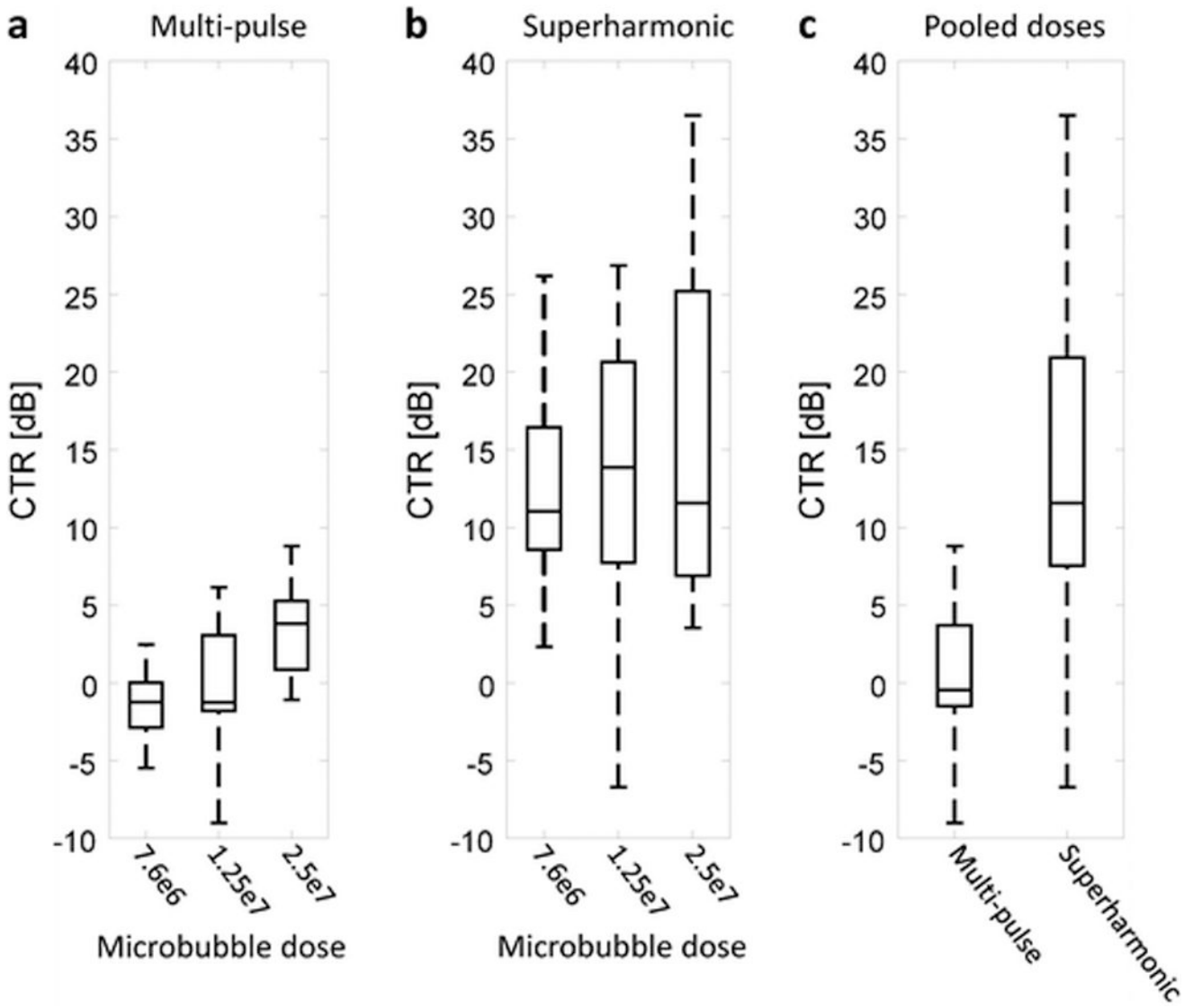

Fig. 3.

Contrast-to-tissue ratio (CTR) for **a** multi-pulse and **b** superharmonic molecular imaging as a function of microbubble dose. **c** CTR pooled across all administered doses indicates significantly higher CTR for superharmonic imaging ($p = 4.9\times10^{-10}$).

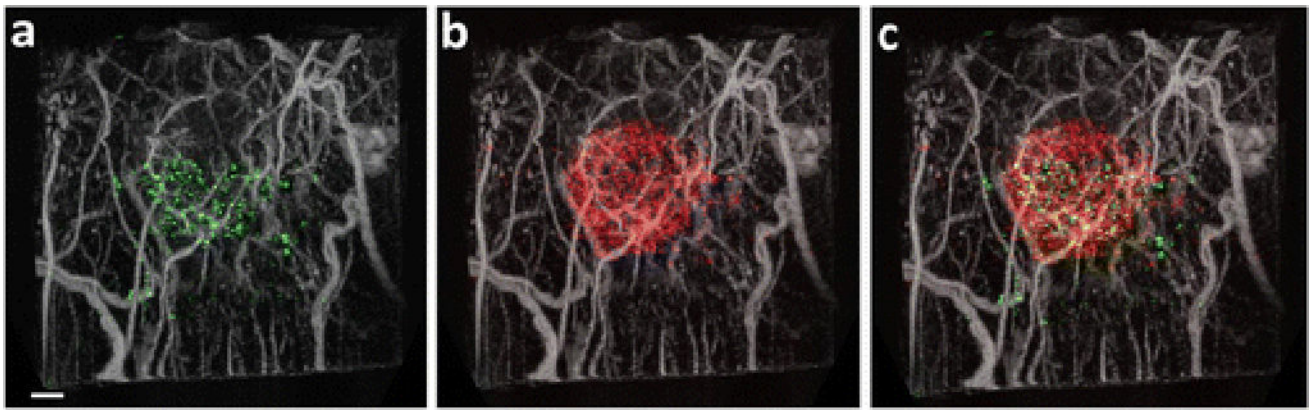

Fig. 4.

Results of acquiring sequential scans of microbubbles targeted to **a** VEGFR2 and **b** both E- and P-selectin. **c** Combining sequential targeted scans using microbubble populations targeted to different markers provides opportunities for analyzing the differential biodistribution of endothelial markers with respect to one another and with respect to microvascular information. MIPs are integrated over the 2.5 cm field of view, encompassing approximately 1 cm of tissue. Scale bar represents 2 mm.

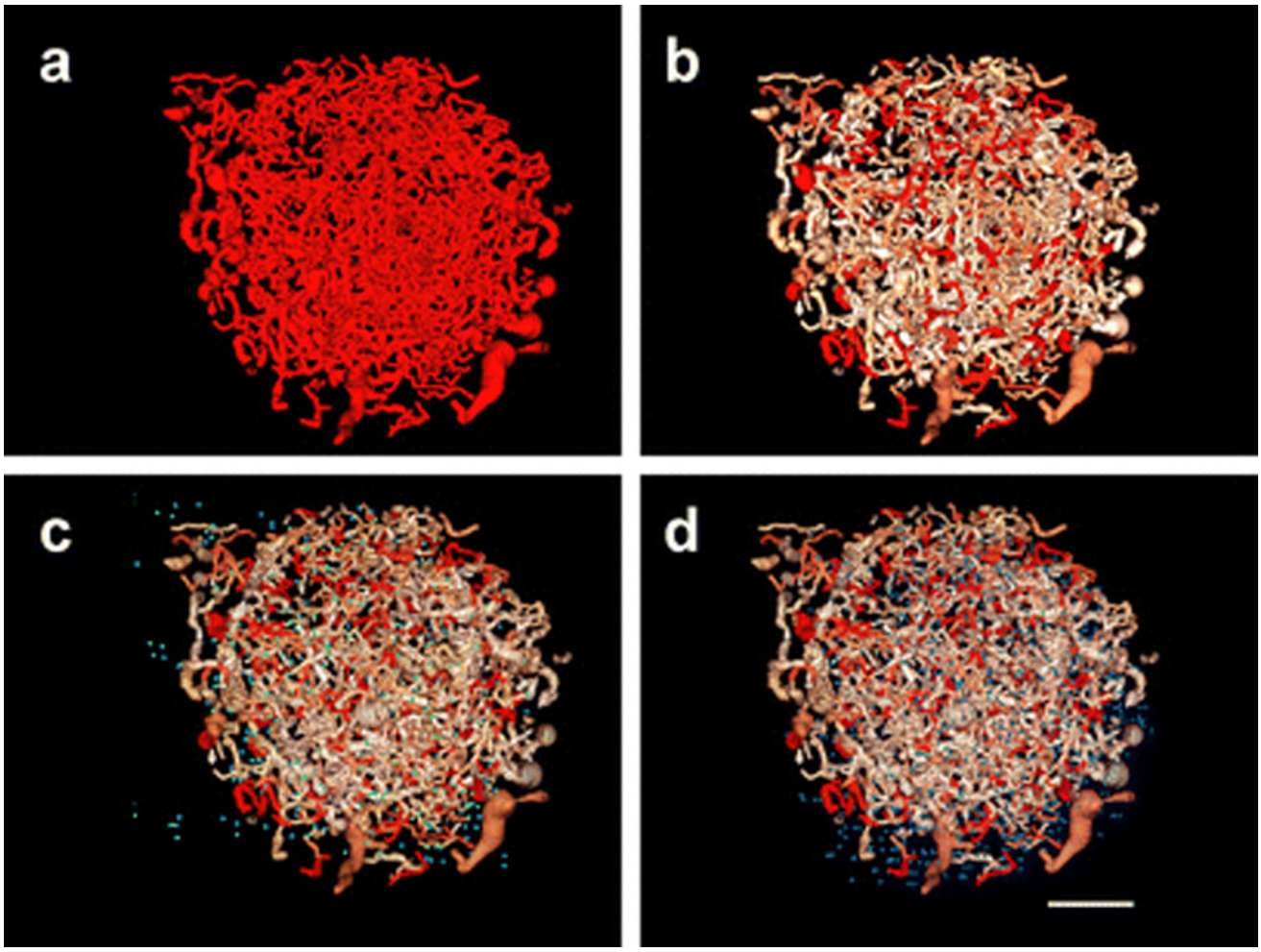

Fig. 5.

Segmented imaging volume containing **a** microvascular imaging data within the tumor, **b** microvascular imaging data with color-coded tortuosity (increasing red indicates increasing tortuosity), **c** microvascular imaging data with color-coded tortuosity and VEGFR2 targeting data (green), and **d** microvascular imaging data with color-coded tortuosity and selectin targeting data (blue). Scale bar represents 2 mm.

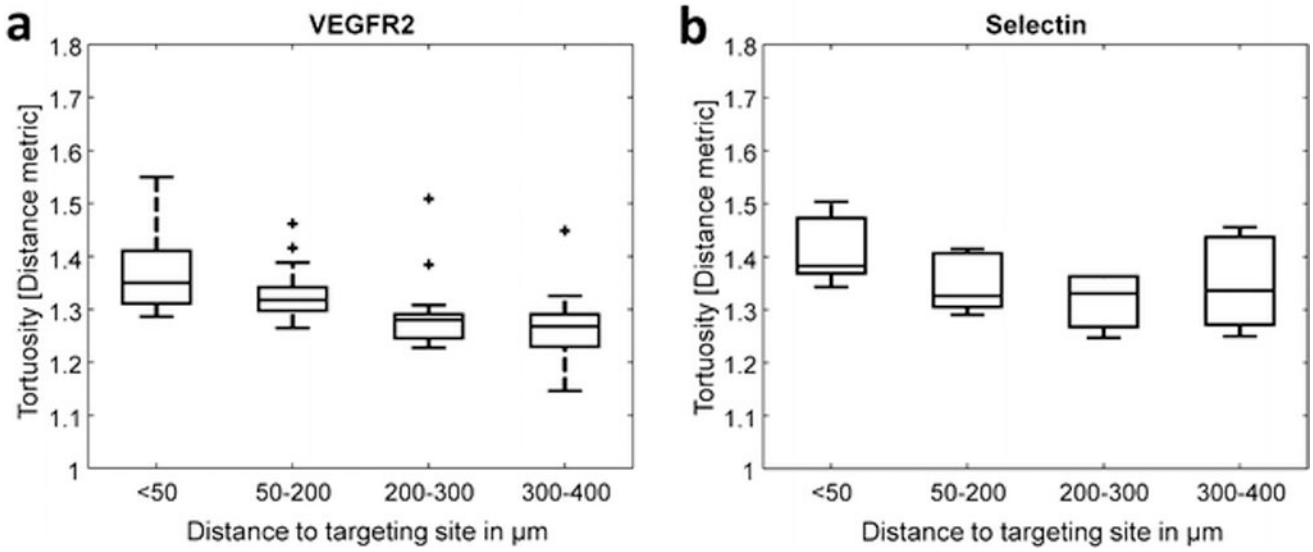

Fig. 6.

Tukey boxplots relating vascular tortuosity and distance between vessels and targeting sites, **a** VEGFR2 (n= 14 animals) and **b** Selectin (5 animals).